Noncollinear spin structure in Fe$_{3+x}$Co$_{3-x}$Ti$_2$ (x = 0, 2, 3) from neutron diffraction

Haohan Wang,[1] Balamurugan Balasubramanian,[1,2] Rabindra Pahari,[1] Ralph Skomski,[1,2] Yaohua Liu,[3]
Ashfia Huq,[3] D. J. Sellmyer,[1,2] and Xiaoshan Xu[1,2]

[1]*Department of Physics and Astronomy, University of Nebraska, Lincoln, Nebraska 68588, USA*
[2]*Nebraska Center for Materials and Nanoscience, University of Nebraska, Lincoln, Nebraska 68588, USA*
[3]*Neutron Scattering Division, Oak Ridge National Laboratory, Oak Ridge, Tennessee 37831, USA*

Neutron powder diffraction has been used to investigate the spin structure of the hard-magnetic alloy Fe$_{3+x}$Co$_{3-x}$Ti$_2$ (x = 0, 2, 3). The materials are produced by rapid quenching from the melt, they possess a hexagonal crystal structure, and they are nanocrystalline with crystallite sizes D of the order of 40 nm. Projections of the magnetic moment onto both the crystalline c axis and the basal plane were observed. The corresponding misalignment angle exhibits a nonlinear decrease with x, which we explain as a micromagnetic effect caused by Fe-Co site disorder. The underlying physics is a special kind of random-anisotropy magnetism that leads to the prediction of $1/D^{1/4}$ power-law dependence of the misalignment angle on the crystallite size.

I. INTRODUCTION

Permanent-magnet material free of rare-earth and other expensive elements is a technologically important research topic, because innovative technologies such as electric cars, wind generators, and medical resonance-imaging work are energy-efficient and easy to operate when using permanent magnets [1–6]. Most top-performing permanent magnets are presently made from rare-earth transition-metal intermetallics such as Nd-Fe-B and Sm-Co [7–9], but supply-chain concerns and raw-materials prices call for replacement options for these often bulky magnets.

The key figure of merit for permanent magnets is the energy product, which describes the magnetostatic energy stored in free space. High-energy-product permanent magnets require high magnetization, high Curie temperatures, and high magnetocrystalline anisotropies [2,10]. Iron and cobalt have very high Curie temperature and magnetization, with Fe being preferred due to its lower raw-materials price. However, the anisotropies of Fe- and Co-based magnets, such as steel magnets, are moderate at best. First, magnetocrystalline anisotropy requires spin-orbit coupling, and this coupling is strongest for heavy elements. Second, the atomic environments in the 3d elements are cubic (bcc Fe, fcc Co) or nearly cubic (hcp Co). Adding small amounts of rare earths, for example through nanostructuring [11–13], is one option, but such structures are extremely difficult and expensive to produce.

Another option is to search for new permanent magnets entirely based on Fe-series (3d) transition-metal elements [14–20]. Some of the structures are potentially highly anisotropic, for example the orthorhombic HfCo$_7$ and the rhombohedral Zr$_2$Co$_{11}$ [21], and there is hope that this structural anisotropy turns into magnetic anisotropy, in spite of the relatively small spin-orbit coupling. A key challenge is that the addition of elements from the first half and from the middle of the 3d series (Ti,Cr,Mn) tends to reduce mag-

netization and Curie temperature. Exploring the full range of ternary and quaternary transition-metal alloys is therefore an important task. Examples of unexpected "hot spots" in phase diagrams are Nd$_2$Fe$_{14}$B [2] and, more recently, partially ordered Mn-Fe-Co [16].

Our focus is on the recently discovered alloy Fe$_{3+x}$Co$_{3-x}$Ti$_2$, whose hexagonal crystal structure has been shown to support uniaxial anisotropies of the order of $K_1 = 1.0$ MJ/m^3 and a magnetization of about 10 kG [22–24], the latter being comparable to SmCo$_5$. Emphasis is on the magnetic anisotropy as a function of the Co content. The dependence of the first uniaxial magnetic anisotropy constant on the number of d electrons tends to be highly nonlinear and needs separate consideration for each alloy system. Substitution of Co by Fe is also interesting from the viewpoint of raw-materials price.

The basics of the micromagnetism of polycrystalline magnets are well-established from the viewpoints of both general magnetism [25] and neutron experiments [26–28]. A particular feature is that easy-plane and easy-axis magnetism are difficult to distinguish in nanocrystalline magnets, both yielding substantial coercivity [29]. Density-functional calculations indicate that rapidly quenched Fe$_{3+x}$Co$_{3-x}$Ti$_2$ exhibits competing anisotropies on an atomic scale, caused by Fe-Co site disorder [22–24]. The effect of this disorder, as well as the spin structure of Fe$_{3+x}$Co$_{3-x}$Ti$_2$, are poorly understood, especially from an experimental viewpoint. Questions are, for example, the possible occurence of easy-cone magnetism [4,10,30] and how atomic-scale easy-plane contributions caused by random-anisotropy disorder [25,31–33] affect the spin structure. In this paper, we study the effect of local disorder in Fe$_{3+x}$Co$_{3-x}$Ti$_2$ (x = 0, 2, and 3) by investigating the spin structure using temperature-dependent neutron powder diffraction (NPD) [34–40] and analyzing the micromagnetic effect of the local disorder on the spin structure. Significant misalignment of spins from the crystalline c axis was observed to increase

TABLE I. Properties of the three samples studied in this work.

Sample	$Fe_3Co_3Ti_2$	Fe_5CoTi_2	Fe_6Ti_2
Mass (g)	4.46	3.41	4.27
Crystallite size (nm)	44 ± 1	44 ± 1	39 ± 2
Thermal expansion coefficient ($10^{-6}\,K^{-1}$)	8.9	8.6	7.9
T_C (K)	586		513
Magnetic moment per unit cell (μ_B)	23 ± 4	25 ± 3	26 ± 2

with the Co concentration, which can be understood as the averaged effect of the local disorder on magnetic anisotropy.

II. EXERIMENTAL APPROACH

Neutron diffraction has long been used to investigate the spin structure of permanent magnets [41]. Spin-polarized neutron experiments were used to investigate the $R_2Fe_{14}B$ magnets, leading to the clarification of its spin structure and to the observation of low-temperature easy-cone magnetism in $Nd_2Fe_{14}B$ [9,30,42,43]. However, $Fe_{3+x}Co_{3-x}Ti_2$ is a nonequilibrium compound and therefore difficult to obtain in single-crystal form. Polycrystalline magnets, including $Nd_2Fe_{14}B$, have been investigated by small-angle neutron scattering (SANS), with emphasis on micromagnetic length scales [26–28]. These measurements are cumbersome to perform over a wide temperature range and yield limited information about the spin structure. In this paper, we use neutron diffraction over the wide angle and temperature range. In particular, the neutron-diffraction selection rules make it possible to determine the alignment between the magnetic moment and the crystalline orientations even in polycrystalline samples.

To produce the sample, we have used a melt-pinning method explained elsewhere [21]. The melt-spun ribbons, which have the compositions $Fe_{3+x}Co_{3-x}Ti_2$ ($x = 0, 2, 3$), were mechanically ground to obtain powders suitable for structural and magnetic characterizations. The high-resolution neutron powder diffraction measurements were carried out between 100 and 600 K without magnetic field using pulsed neutron beams at the beamline POWGEN in the Spallation Neutron Source at the Oak Ridge National Laboratory. The sample masses for the neutron diffraction measurements were 4.46 g ($Fe_3Co_3Ti_2$), 3.41 g (Fe_5CoTi_2), and 4.27 g (Fe_6Ti_2), as shown in Table I. The diffraction spectra were analyzed using the Rietveld method [44] with the FULLPROF program [45]. The bulk magnetization measurements were carried out using a Quantum Design superconducting quantum interference device (SQUID) magnetometer and a physical property measurement system (PPMS).

III. RESULTS AND DISCUSSION

In this section, we present and analyze the results of the neutron diffraction experiments. Structurally, we focus on the lattice constants as functions of composition x and temperature T, and on the crystallite-size determination from the width of the diffraction peaks. The separated nuclear and magnetic contributions to the neutron diffraction are used to extract the magnitude of the magnetic moment and its direction with respect to the local c-axis.

A. Crystallographic structure

The $Fe_{3+x}Co_{3-x}Ti_2$ alloys crystallize in the hexagonal structure of Fig. 1(a), which has the space group $P\bar{6}m2$ (point group C_{3h}). Figure 1(b) shows the 600 K diffraction intensities of $Fe_{3+x}Co_{3-x}Ti_2$ ($x = 0, 2, 3$) as a function of the d spacing of the lattice planes. The intensities are scaled by the sample mass and by the charge deposited by the proton beam on the liquid mercury target. The diffraction spectra are consistent with the hexagonal structure of polycrystalline $Fe_{3+x}Co_{3-x}Ti_2$ [22]; the Miller indices (h, k, l) of selected peaks are marked accordingly. The significant differences between the diffraction intensities of the samples are due to the large difference between the neutron coherent scattering length of Co and Fe [46].

The powder samples consist of randomly oriented crystallites whose size D can be estimated from the widths of the diffraction peaks. Provided that the instrument broadening is much smaller than the peak width, $D \approx 2d^2/\Delta d$ [23], where Δd is the peak's full width at half-maximum. Figure 2(a) shows the temperature dependence of the crystallite size D, using the well-separated peaks (014), (024), (018), (026), and (034). We obtained crystallite sizes of about 44 nm for Fe_6Ti_2 and Fe_5CoTi_2, whereas the crystallite size of the $Fe_3Co_3Ti_2$ sample is around 39 nm. The corresponding errors of 1–2 nm (Table I) were calculated from the dispersion of the results of different peaks. Our Williamson-Hall analysis reveals a very small microstrain of only about 0.1%, which has little effect on the estimated crystallite size [47]. The crystallite sizes do not exhibit any obvious temperature dependence, suggesting that the microstructures are stable over the temperature range of the measurements.
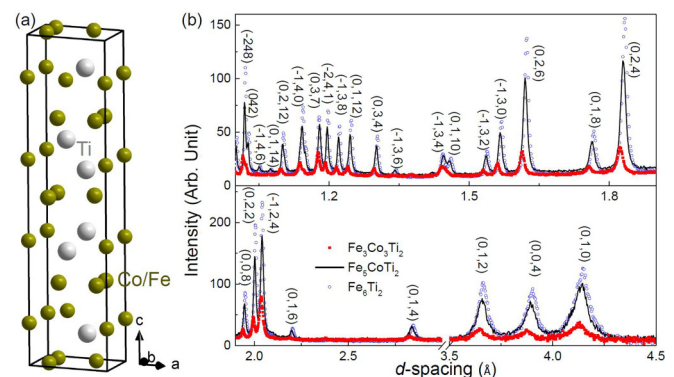

FIG. 1. Crystal structure and neutron diffraction patterns: (a) unit cell of hexagonal $Fe_{3+x}Co_{3-x}Ti_2$ and (b) neutron powder diffraction spectra for different composition, measured at 600 K and scaled by incident neutron counts and sample mass.
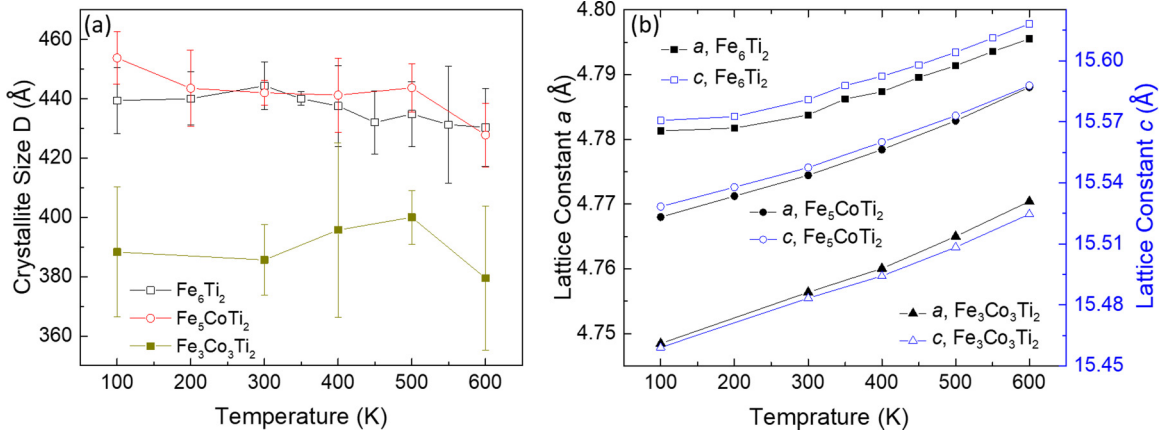
FIG. 2. Temperature dependence of crystallographic properties: (a) crystallite size calculated from the diffraction peak widths and (b) lattice constants.

The lattice constants and their temperature dependence, Fig. 2(b), were obtained by fitting the diffraction spectra with the Rietveld method implemented in the software FULLPROF (see Fig. S1) [45,48]. The lattice constants of $Fe_{3+x}Co_{3-x}Ti_2$ increase with x, which is consistent with the smaller atomic radius of Co compared with that of Fe. For each compound, the temperature dependences of the lattice constants a and c are similar. For $Fe_3Co_3Ti_2$ and Fe_5CoTi_2, the thermal expansion appears to be linear in the range 100–600 K, while for Fe_6Ti_2 the thermal expansion is linear only above 300 K, indicating that Fe_6Ti_2 may have a substantially higher Debye temperature. The linear thermal expansion coefficients between 300 and 600 K are about 8×10^{-6}/K in both the a and c directions (Table I). These values are somewhat smaller than those for Co and Fe, 13×10^{-6}/K and 11.8×10^{-6}/K, respectively, but close to that of Ti, 8.6×10^{-6}/K [49].

B. Spin structure (magnitude and direction of magnetic moment)

Neutron diffraction can be used to trace the magnitude and direction of the magnetic moment after careful separation of the magnetic contribution from the nuclear contribution. The nuclear (n) and magnetic (m) parts of the powder neutron diffraction are

$$I_n = ABF_n^2 e^{-2W(T)} \tag{1}$$

and

$$I_m = ABF_m^2 e^{-2W(T)}, \tag{2}$$

where A is a common constant factor and B is the multiplicity, which depends on the diffracting plane indicated by (h, k, l). The Debye-Waller factor $e^{-2W(T)}$ comes from the effect of thermal fluctuation of atomic positions on the diffraction, where $W(T)$ increases with temperature [23].

In the nuclear part, $F_n = \Sigma_i [f_i \exp(i\mathbf{K} \cdot \mathbf{r}_i)]$ is the crystal structure factor and i is the index of atoms in the unit cell of the crystal structure, where the positions of the Fe and Co atoms are approximated by the ordered sublattices. The position of the ith atom in the unit cell is denoted by $\mathbf{r}_i$; $f(\text{Fe}) = 9.45$ fm, $f(\text{Co}) = 2.49$ fm, $f(\text{Ti}) = -3.438$ fm are the neutron coherent scattering lengths of the elements [46];

$\mathbf{K}$ is the neutron wave-vector transfer, which can be expressed in terms of the Miller indices h, k, and l in the reciprocal space that represents the diffraction planes.

For the magnetic part, if the magnetic structure in every unit cell is the same, one has [35,39]

$$F_m^2 = \tfrac{1}{2}(\gamma r_0 g)^2 \Sigma_{\alpha,\beta}(\delta_{\alpha\beta} - K_\alpha K_\beta / K^2) \Sigma_{i,j} f_i'(\mathbf{K}) f_j'(\mathbf{K})$$
$$\times \exp[i\mathbf{K}(\mathbf{r}_i - \mathbf{r}_j)] S_{i\alpha} S_{j\beta}. \tag{3}$$

Here $\alpha, \beta \in \{x, y, z\}$, $\delta_{\alpha\beta}$ is the unity matrix (Kronecker symbol), K_α is the projection of $\mathbf{K}$ along the α-direction, S_{ia} is the projection of the spin $\mathbf{S}_i$ of the ith atom onto the α-direction, and $f_i'(\mathbf{K})$ is the magnetic form factor, which depends on the type of the magnetic atom [50]. For the Landé factor we assume $g = 2$, because the orbital moment of $3d$ alloys is largely quenched. $\gamma = 1.913$ and the classical electron radius $r_0 = 2.818 \times 10^{-15}$ m.

To separate the nuclear and the magnetic contributions, we first estimated the Curie temperature T_C using the temperature-dependent magnetometry during heating in a field of 1 kOe, as shown in Fig. 3(a). The T_C extracted using linear extrapolation is shown in Table I. The neutron spectra above 500 K, therefore, contain only minimal magnetic contribution, as also shown in Figs. 3(b)–3(d).

To evaluate the nuclear contribution to the diffraction intensity, we have exploited that the temperature dependence of I_n comes from the Debye-Waller factor $e^{-2W(T)}$, so long as there is no structural transition at high temperature. Based on $W(T) = \beta T/(4d^2)$, we fit the experimental values of $\ln[I(d, T)]d^2$ with a linear relation with T above 500 K [23], which yields β-values of 2.5, 2.0, and 12.0×10^{-4} Å^2/K for Fe_6Ti_2, Fe_5CoTi_2, and $Fe_3Co_3Ti_2$, respectively. The nuclear contribution can then be obtained from $I_n = I_n(T_1) \exp[-2W(T) + 2W(T_1)]$ and subtracted, where $T_1 = 600$ K is a reference temperature.

Some examples of diffraction peaks at various temperature are shown in the Supplemental Material (see Fig. S2) [48]. Figures 3(a)–3(c) show the integrated intensities of the magnetic part for the (008) and (010) peaks. All peak intensities in Figs. 3(a)–3(c) decrease with increasing temperature, as expected from the temperature dependence of the magnetization. In Figs. 3(b)–3(d), the (008) intensities are much smaller
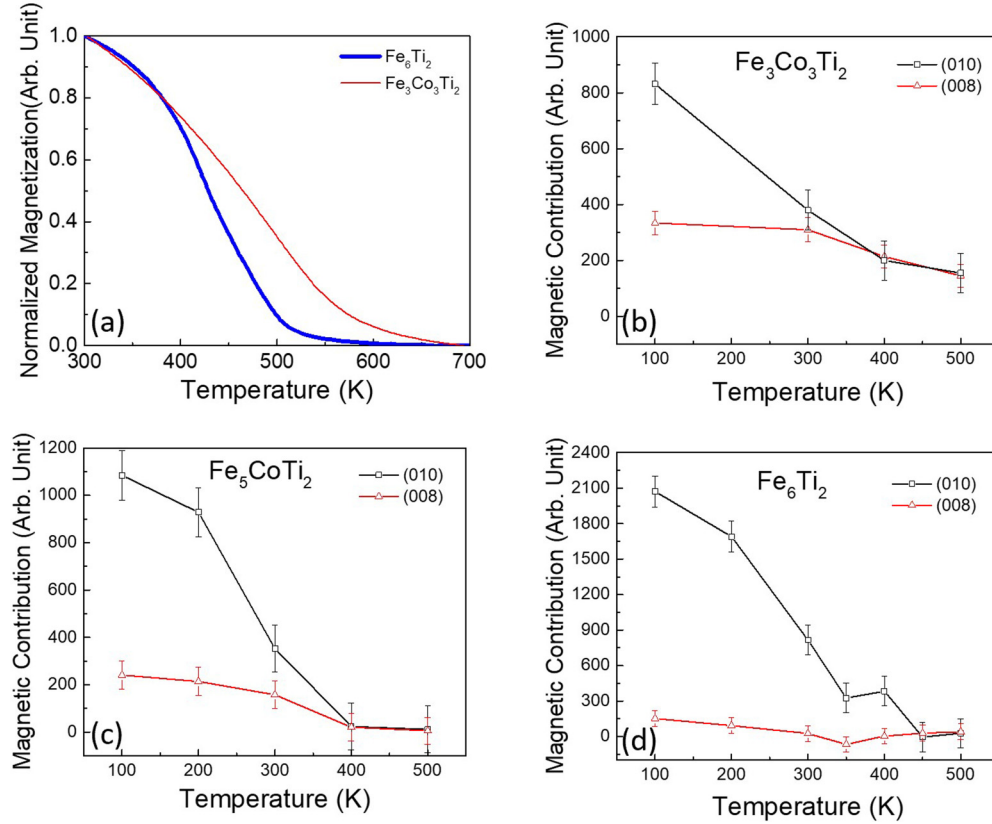
FIG. 3. Temperature dependence of magnetization: (a) Normalized magnetization measured using magnetometry during heating in a 1 kOe field and (b)–(d) magnetic contribution of neutron diffraction intensity.

than the (010) intensities. Magnetic neutron diffraction detects only the part of the magnetic moment perpendicular to K, so that the less intense (008) diffraction suggests that the magnetic moment is more aligned to the c axis.

For a quantitative discussion, we assume that all spins in one unit cell are aligned along the same axis, so that Eq. (3) simplifies to

$$I_m = \frac{1}{2}A(g\gamma r_0)^2 \exp\left[-2W(T)\right]B(\mathbf{K})|\Sigma_i[f_i'(\mathbf{K})$$
$$\times \exp(i\mathbf{K}\times\mathbf{r}_i)]|^2 S^2 q^2(\mathbf{K}). \quad (4)$$

Here $q^2(\mathbf{K}) = 1 - [\mathbf{S}\cdot\mathbf{K}/(SK)]^2$ means that neutron diffraction selects out the perpendicular component of the magnetic moment, and S is the average spin per atom.

With the nuclear and magnetic contributions separated, we can now estimate the magnitude and the directions of the magnetic moment. While the magnitude can be estimated by comparing the intensity of the nuclear and magnetic contributions, the direction can be estimated by comparing magnetic diffraction intensities of different K.

First, we analyze the direction of the magnetic moment by estimating $q^2(\mathbf{K})$. Since $B(\mathbf{K})$, $\Sigma_i\exp(j\mathbf{K}\cdot\mathbf{r}_i)$, and $f_i'(\mathbf{K})$ are known, one can calculate the product $AS^2q^2(\mathbf{K})$ from Eq. (4) and the magnetic contribution in Fig. 3. The ratio $q^2(010)/q^2(008)$ can then be obtained. Introducing the angle θ between the magnetic moment and the K vector, $q^2(\mathbf{K}) = \sin^2\theta$. The angles between a certain vector and three orthogonal coordinates in space satisfy $\Sigma_\alpha \sin^2\theta_\alpha = 2$. Since the vector (010) is perpendicular to the vector (008) and the

vectors within the basal plane are equivalent due to the crystal symmetry, one has $2q^2(010) + q^2(008) = 2$. Using this relation and the ratio $q^2(010)/q^2(008)$, we obtained $q^2(010)$ and $q^2(008)$ for all three compounds. To quantify the spin direction, we calculated the average angle $\langle\theta_c\rangle$ between the magnetic moment and the c axis using $q^2(008) = \sin^2\langle\theta_c\rangle$ at 100 K, which is displayed in Fig. 4(a).

Next, we analyze the magnitude S^2 by comparing the nuclear and magnetic contributions. With $q^2(\mathbf{K})$ being calculated, the ratio between the magnetic contribution and the nuclear contribution is

$$\frac{I_m}{I_n} = \frac{1}{2}(g\gamma r0)^2 |\Sigma_i[f_i(\mathbf{K})\exp(i\mathbf{K}\cdot\mathbf{r}_i)]|^2 S^2 q^2(\mathbf{K})$$
$$/|\Sigma_i[f_i\exp(i\mathbf{K}\cdot\mathbf{r}_i)]|^2, \quad (5)$$

where S^2 is the only unknown variable. This procedure yields the respective magnetic moment values per Co/Fe $0.81 \pm 0.03\,\mu_B$, $0.64 \pm 0.06\,\mu_B$, and $0.61 \pm 0.06\,\mu_B$ for Fe_6Ti_2, Fe_5CoTi_2, and $Fe_3Co_3Ti_2$ at 100 K. The corresponding magnetic moment per unit cell is $29 \pm 1\,\mu_B$, $23 \pm 2\,\mu_B$, and $22 \pm 2\,\mu_B$ for Fe_6Ti_2, Fe_5CoTi_2, and $Fe_3Co_3Ti_2$ respectively. These value are consistent with the saturation magnetization previously [24] extracted from the magnetometry measurements at 10 K, as shown in Fig. 4(b).

C. Micromagnetic analysis

The most interesting experimental result is that the average misalignment angle $\langle\theta_c\rangle$ increases significantly with Co
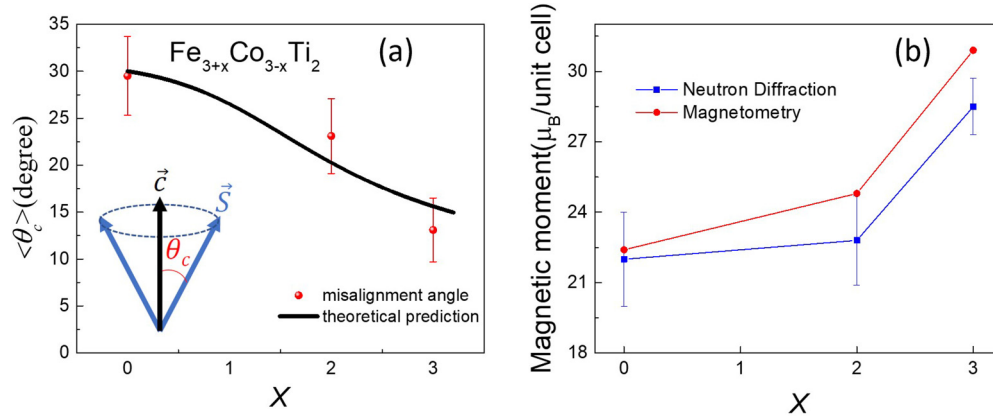
FIG. 4. Dependence of magnetic moment on chemical composition x in $Fe_{3+x}Co_{3-x}Ti_2$. (a) Direction of moment measured using neutron experiment at 100 K; the line is a theoretical prediction (see text). (b) Magnitude of moment measured using magnetometry at 10 K[24] and measured using neutron diffraction at 100 K.

content, as shown in Fig. 4(a). We explain this trend as a combined intrinsic and micromagnetic effect. Intrinsically, the substitution of Co for Fe creates chemical disorder (site disorder), and this site disorder leads to a distribution of the local anisotropy. The corresponding random-anisotropy contribution will be shown in this subsection to enhance $\langle \theta_c \rangle$.

In general, the direction of a spin with respect to the crystalline axes is related to the magnetocrystalline anisotropy-energy density η [25]. The present alloys crystallize in a hexagonal structure and therefore they exhibit

$$\eta = K_1 \sin^2\theta_c + K_2 \sin^4\theta_c + K_3 \sin^6\theta_c + K_3' \sin^6\theta_c \cos\phi.$$

(6)

Here K_1, K_2, and K_3 are the second-, fourth-, and sixth-order uniaxial anisotropy constants and K_3' describes the sixth-order in-plane anisotropy of the crystals. The lower-order in-plane anisotropies K_1' and K_2' are zero in hexagonal crystals. The sixth-order anisotropy constants K_3 and K_3' tend to be much smaller than K_1 and are normally neglected. Depending on the values of K_1 and K_2, the spin structure may then be of the easy-cone type, where the macroscopic spin direction forms an angle θ_c with the c-axis [10,25,30]. Easy-cone magnetism leads to characteristic singularities in the hysteresis loop [30], but our previous magnetization measurements [20] do not show any sign of such singularities. We therefore neglect K_2 in the following analysis. So, the only surviving term is $K_1 \sin^2\theta$.

For an isolated magnetic crystallite with a homogeneous K_1, depending on the sign of K_1, the preferred magnetization direction is easy-axis ($\theta_c = 0$, $K_1 > 0$) or easy-plane ($\theta_c = \pi/2$, $K_1 < 0$). These two scenarios correspond to the left and right parts of Fig. 5(a), respectively. However, the spin direction can be distorted at the boundary between crystallites with randomly oriented crystalline axes due to their exchange coupling. Exchange energy between neighboring spins is typically much stronger than the magnetic anisotropy energy. In the present case, the temperature equivalents of anisotropy and exchange energies are of the orders of 0.1 and 500 K, respectively. The strong exchange interaction means that neighboring spins are almost parallel [51], as in Fig. 5(b). At the boundaries of crystallites of misaligned crystalline

axes, the exchange energy, which favors parallel spins, and the anisotropy energy, which favors spin alignment along the crystalline axes, compete and generate inhomogeneous magnetization typically at the nanoscale, as discussed below.

At the crystallite boundary, the spins deviate from the crystalline axes due to the exchange coupling with spins in neighboring crystallites. The misalignment angle decays approximately exponentially with the distance r from the crystallite boundary and obeys

$$\Delta\theta_c(r) \sim \exp(-r/\delta),$$ (7a)

$$\delta = (A'/K_1)^{1/2},$$ (7b)

where A' is the exchange stiffness [25]. The average angular deviation from the crystalline c axis is obtained by integrating Eq. (7a) over r. When $\delta/D \ll 1$, Eq. (7a) suggests that the change in spin direction is confined to a boundary region of thickness δ, as illustrated in Fig. 5(c). In this limit, taking into account that the surface proportion of the crystallites is approximately equal to $3\delta/D$, the integration leads to

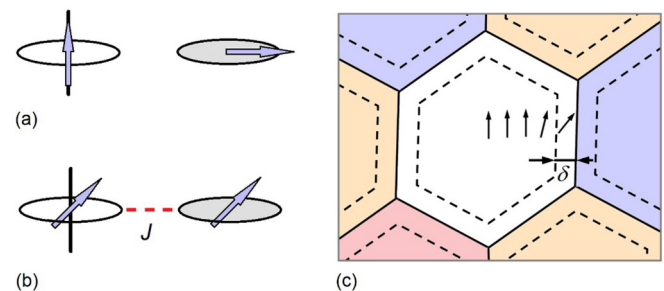$$\langle \theta_c \rangle = (3\delta/D)\langle \theta_c \rangle_o.$$ (8)

FIG. 5. Spin directions in polycrystalline $Fe_{3+x}Co_{3-x}Ti_2$: (a) and (b) intrinsic (atomic-scale) effects and (c) extrinsic (nanoscale) effects. The thick lines in (a) and (b) show the c-axis, whereas the gray circles symbolize the $a - b$ plane. Published DFT anisotropy calculations [24] support the coexistence of easy-axis and easy-plane anisotropies [(a) and (b)]. Spin structures (a) and (b) differ by the absence or presence of interatomic exchange, respectively; the physically realized case is (b).

Here the average $\langle\theta_c\rangle_o = 57.3°$ is the *c*-axis misalignment angle between randomly oriented crystallites, which follows from $\sin^2\langle\theta_c\rangle_o = 2/3$. Taking $\delta = \delta_o \approx 3$ nm, calculated from the experimental K_1 in Ref. [24] and $A \approx 10$ pJ/m [25], and $D = 40$ nm yields $\langle\theta_c\rangle = 13°$. This estimate is in the right ballpark but at the lower end of the experimental results, so misalignment near crystallite boundaries explains the experimental data only partly. A refined analysis needs to take into account that there is a competition between atomic-scale easy-axis ($K_1 > 0$) and easy-plane ($K_1 < 0$) anisotropies due to Co-Fe antisite disorder, as indicated by DFT [24].

The DFT calculations (second paragraph on p. 5 in Ref. [24]) indicate that K_1 becomes zero near $x_c = 0.9$. According to Eqs. (7b) and (8), this zero corresponds to infinite values of δ and $\langle\theta_c\rangle$, more than explaining the increase of $\langle\theta_c\rangle$ compared to the Fe-rich side. However, this ideal soft-magnetic limit is not realized in practice, and the effective anisotropy entering Eq. (7b) is always nonzero. First, the coexistence of atomic-scale easy-plane and easy-axis anisotropy contributions creates a random-anisotropy problem. Even in the limit $\langle K_1\rangle = 0$, where easy-axis and easy-plane contributions cancel each other, atomic-scale anisotropy fluctuations, $\delta K^2 > 0$, keep δ finite [25,33].

For simplicity, we assume that a fraction $1 - p$ of all Fe/Co atoms has an easy-axis anisotropy of energy density $K_o\sin^2\theta_c$ and the remaining fraction p has an easy-plane anisotropy, $-K_p\sin^2\theta_c$. Note that K_o and K_p are both positive in this definition, both of the order of 0.5 MJ/m^3. Straightforward anisotropy averaging yields

$$\langle K_1\rangle = (1-p)K_o - pK_p, \tag{9a}$$

$$\langle K_1^2\rangle = (1-p)K_o^2 + pK_p^2. \tag{9b}$$

The anisotropy fluctuations are described by an energy δE obeying

$$\delta E^2 = \int \langle K_1(\boldsymbol{r})K_1(\boldsymbol{r}')\rangle d\boldsymbol{r}\, d\boldsymbol{r}', \tag{10}$$

where the integration is over one crystallite. Near $x = x_c$, assuming that the anisotropies of neighboring atoms are uncorrelated, we can write

$$\langle K_1(\boldsymbol{r})K_1(\boldsymbol{r}')\rangle = V_o\delta(\boldsymbol{r}-\boldsymbol{r}')\langle K_1^2\rangle. \tag{11}$$

In this equation, V_o is the crystal volume per Fe/Co atom. Inserting Eq. (11) into Eq. (10) and performing the integration yields

$$\delta E^2 = V_o V_g\langle K_1^2\rangle, \tag{12}$$

where V_g is the crystallite volume. The energy δE can be written in terms of a net anisotropy K_{RA} arising from the random anisotropy fluctuations: $\delta E = K_{RA} V_g$.

To determine δE, we need to evaluate $\langle K_1^2\rangle$ at x_c. Since $\langle K_1\rangle(p_c) = 0$ and $p_c = K_o/(K_o + K_p)$, Eq. (9b) becomes

$$\langle K_1^2\rangle(x_c) = K_o K_p. \tag{13}$$

Combining $\delta E = K_{eff} V_g$ with Eqs. (12) and (13) yields

$$K_{RA} = \sqrt{\frac{V_o}{V_g}K_o K_p}. \tag{14}$$

This K_{RA} prevents δ from becoming infinite. However, $V_o/V_g = (d_o/D)$ [3], where $d_o \approx 0.29$ nm is the distance between Fe and Co nearest neighbors and $D \approx 40$ nm. This makes K_{eff} very small and the $\delta_{RA} = (A'/K_{RA})^{1/2}$ very large, several times the crystallite size. Explicitly, $\delta_{eff} = (D/d_o)^{3/4}\delta_o$. This power-law dependence, $\delta_{RA} \sim D^{3/4}$, is remarkable, because it means that the random-anisotropy effects vanish very slowly in the macroscopic limit, $\langle\theta_c\rangle \sim D^{-1/4}$. For example, increasing the crystallite size from 40 to 1000 nm reduces the corresponding $\langle\theta_c\rangle$ value by a factor of only 2.2.

In reality, crystallite boundaries are a big perturbation compared to the small energies δE responsible for the large values of δ_{RA}, because there are crystallite-boundary anisotropies and shape anisotropies related to the shape of individual crystallites. These two effects may be lumped into a crystallite anisotropy K_G which obeys $K_o \approx K_p > K_G \gg K_{RA}$. Simplifying somewhat for clarity, K_o, K_G, and K_{RA} reflect hard-, semihard-, and soft-magnetic anisotropy contributions. The atomic-scale anisotropies K_o and K_p compete against and effective anisotropy $K_G + K_{RA} \approx K_G$. Anisotropy contributions much smaller than K_G do not affect the spin structure, so that K_G yields a cutoff $\delta_{eff} = (A'/K_G)^{1/2}$ limiting the prediction of Eq. (8).

The measured angle $\langle\theta_c\rangle$ depends on $\langle K_1\rangle(x) = (x–0.9)K'$, where $K' \approx 0.2$ MJ/m^3 [24], and on K_G. To fit the experimental data, we need a mathematical function $K_{eff}(x)$ that ensures a constant value K_B for small x and $(x - 0.9)K'$ for large x. It is easy to show that the function

$$K_{eff} = K_B\ln\{e + \exp[K'/K_B(x - 0.9)]\} \tag{15}$$

satisfies this condition. The dashed line in Fig. 4(a) combines Eqs. (7b) and (8) with Eq. (15), showing

$$\langle\theta_c\rangle = 3/D[A'/K_{eff}(x)]^{1/2}\langle\theta_c\rangle_o.$$

The fitting yield $K_B = 0.541$ $K' \approx 0.1$ MJ/m^3, which is typical [25] for shape anisotropies.

IV. CONCLUSIONS

In summary, we have used neutron powder diffraction to investigate the magnetic structure and magnetic anisotropy of polycrystalline Fe-Co-Ti alloys. The most interesting finding in this work is the nonzero misalignment angle $\langle\theta_c\rangle$, which indicates a nonzero projection of the magnetic moment onto both the *c* axis and the basal plane, and the dependence of $\langle\theta_c\rangle$ on the Co content. We explain these findings as a type of random-anisotropy effect caused by Co-Fe chemical disorder that translates into a micromagnetic spin canting. The added Co leads to a K_1 distribution, that is, to an atomic-scale coexistence of easy-axis and easy-plane anisotropies, and this distribution enhances the width δ in Fig. 5 and therefore the angle $\langle\theta_c\rangle$. An interesting feature is the weak power-law dependence of δ on D, which explains why the atomic-scale chemical-disorder effect is visible on a scale of about 40 nm.

[1] K. J. Strnat, J. Magn. Magn. Mater. **7**, 351 (1978).

[2] K. J. Strnat and R. M. W. Strnat, J. Magn. Magn. Mater. **100**, 38 (1991).

[3] O. Gutfleisch, M. A. Willard, E. Brück, C. H. Chen, S. G. Sankar, and J. P. Liu, Adv. Mater. **23**, 821 (2011).

[4] R. Skomski, P. Manchanda, P. Kumar, B. Balamurugan, A. Kashyap, and D. J. Sellmyer, IEEE Trans. Magn. **49**, 3215 (2013).

[5] R. Skomski and J. M. D. Coey, Scr. Mater. **112**, 3 (2016).

[6] J. Cui, M. Kramer, L. Zhou, F. Liu, A. Gabay, G. Hadjipanayis, B. Balasubramanian, and D. Sellmyer, Acta Mater. **158**, 118 (2018).

[7] K. Kumar, J. Appl. Phys. **63**, R13 (1988).

[8] R. Kumar, W. B. Yelon, and C. D. Fuerst, J. Appl. Phys. **63**, 3725 (1988).

[9] J. F. Herbst, Rev. Mod. Phys. **63**, 819 (1991).

[10] R. Skomski and J. M. D. Coey, *Permanent Magnetism* (Institute of Physics Publishing, Bristol, 1999).

[11] R. Skomski and J. M. D. Coey, Phys. Rev. B **48**, 15812 (1993).

[12] S. D. Bader, Rev. Mod. Phys. **78**, 1 (2006).

[13] N. Jones, Nature (London) **472**, 22 (2011).

[14] J. M. D. Coey, IEEE Trans. Magn. **47**, 4671 (2011).

[15] J. M. D. Coey, J. Phys. Condens. Matter **26**, 064211 (2014).

[16] R. J. Snow, H. Bhatkar, A. T. N'Diaye, E. Arenholz, and Y. U. Idzerda, Appl. Phys. Lett. **112**, 072403 (2018).

[17] L. H. Lewis, F. E. Pinkerton, N. Bordeaux, A. Mubarok, E. Poirier, J. I. Goldstein, R. Skomski, and K. Barmak, IEEE Magn. Lett. **5**, 1 (2014).

[18] B. Balasubramanian, B. Das, R. Skomski, W. Y. Zhang, and D. J. Sellmyer, Adv. Mater. **25**, 6090 (2013).

[19] L. Néel, J. Pauleve, R. Pauthenet, J. Laugier, and D. Dautreppe, J. Appl. Phys. **35**, 873 (1964).

[20] S. Sanvito, C. Oses, J. Xue, A. Tiwari, M. Zic, T. Archer, P. Tozman, M. Venkatesan, M. Coey, and S. Curtarolo, Sci. Adv. **3**, e1602241 (2017).

[21] B. Balamurugan, B. Das, W. Y. Zhang, R. Skomski, and D. J. Sellmyer, J. Phys. Condens. Matter **26**, 064204 (2014).

[22] J. Zhang, M. C. Nguyen, B. Balasubramanian, B. Das, D. J. Sellmyer, Z. Zeng, K.-M. Ho, and C.-Z. Wang, J. Phys. D **49**, 175002 (2016).

[23] X. Xu, X. Zhang, Y. Yin, B. Balasubramanian, B. Das, Y. Liu, A. Huq, and D. J. Sellmyer, J. Phys. D **50**, 025002 (2017).

[24] B. Balasubramanian, B. Das, M. C. Nguyen, X. Xu, J. Zhang, X. Zhang, Y. Liu, A. Huq, S. R. Valloppilly, Y. Jin, C.-Z. Wang, K.-M. Ho, and D. J. Sellmyer, APL Mater. **4**, 116109 (2016).

[25] R. Skomski, J. Phys. Condens. Matter **15**, R841 (2003).

[26] J. Weissmüller, A. Michels, J. G. Barker, A. Wiedenmann, U. Erb, and R. D. Shull, Phys. Rev. B **63**, 214414 (2001).

[27] A. Michels and J. Weissmueller, Rep. Prog. Phys. **71**, 066501 (2008).

[28] A. Michels, J. Phys. Condens. Matter **26**, 383201 (2014).

[29] B. Balasubramanian, P. Manchanda, R. Skomski, P. Mukherjee, S. R. Valloppilly, B. Das, G. C. Hadjipanayis, and D. J. Sellmyer, Appl. Phys. Lett. **108**, 152406 (2016).

[30] F. Bolzoni, O. Moze, and L. Pareti, J. Appl. Phys. **62**, 615 (1987).

[31] E. Callen, Y. J. Liu, and J. R. Cullen, Phys. Rev. B **16**, 263 (1977).

[32] D. J. Sellmyer and S. Nafis, Phys. Rev. Lett. **57**, 1173 (1986).

[33] G. Herzer, J. Magn. Magn. Mater. **112**, 258 (1992).

[34] C. G. Shull, W. A. Strauser, and E. O. Wollan, Phys. Rev. **83**, 333 (1951).

[35] B. W. Roberts, Phys. Rev. **104**, 607 (1956).

[36] P. B. Braun and J. A. Goedkoop, Acta Crystallogr. **16**, 737 (1963).

[37] A. F. Andresen, W. Halg, P. Fischer, and E. Stoll, Acta Chem. Scand. **21**, 1543 (1967).

[38] Y. C. Yang, W. W. Ho, C. Lin, J. L. Yang, H. M. Zhou, J. X. Zhu, X. X. Zeng, B. S. Zhang, and L. Jin, J. Appl. Phys. **55**, 2053 (1984).

[39] G. L. Squires, *Introduction to the Theory of Thermal Neutron Scattering* (Cambridge University Press, Cambridge, 2013).

[40] J. Cui, J. P. Choi, G. Li, E. Polikarpov, J. Darsell, M. J. Kramer, N. A. Zarkevich, L. L. Wang, D. D. Johnson, M. Marinescu, Q. Z. Huang, H. Wu, N. V. Vuong, and J. P. Liu, J. Appl. Phys. **115**, 17A743 (2014).

[41] J. W. Cable and E. O. Wollan, Phys. Rev. **165**, 733 (1968).

[42] D. Givord, H. S. Li, and F. Tasset, J. Appl. Phys. **57**, 4100 (1985).

[43] J. F. Herbst and W. B. Yelon, J. Appl. Phys. **57**, 2343 (1985).

[44] H. M. Ritveld, J. Appl. Crystallogr. **2**, 65 (1969).

[45] J. Rodríguez-Carvajal, Phys. B **192**, 55 (1993).

[46] V. F. Sears, *Neutron Scattering Lengths and Cross Sections* (Taylor & Francis, London, 1992).

[47] H. Neves Bez, K. K. Nielsen, A. Smith, P. Norby, K. Ståhl, and C. R. H. Bahl, Appl. Phys. Lett. **109**, 051902 (2016).

[48] See Supplemental Material at http://link.aps.org/supplemental/10.1103/PhysRevMaterials.3.064403 for more information on diffraction spectra and fit and magnetometry.

[49] D. R. Lide, *CRC Handbook of Chemistry and Physics: A Ready-Reference Book of Chemical and Physical Data* (CRC, Boca Raton, FL, 1994).

[50] E. Prince and I. U. of Crystallography, *International Tables for Crystallography. Volume C* (Wiley, Chichester, 2011).

[51] S. Chikazumi, *Physics of Magnetism* (Krieger, Malabar, FL, 1986).